J Mater Sci (2010) 45:4778–4789
DOI 10.1007/s10853-010-4595-0

ULTRAFINE GRAINED MATERIALS

Work-hardening stages of AA1070 and AA6060 after severe plastic deformation

Matthias Hockauf · Lothar W. Meyer

Received: 12 February 2010 / Accepted: 4 May 2010 / Published online: 25 May 2010

Abstract Based on the concept of work-hardening for fcc metals, the commercially pure aluminum AA1070 (soft annealed) and the aluminum alloy AA6060 (peak-aged) were investigated. Equal-channel angular pressing (ECAP) was used to introduce very high strains and an ultrafine-grained microstructure. Compression tests were performed in a wide range of strain rates between 10^{-4} and 10^{3} s^{-1} subsequently. The results show that strain path and the corresponding dislocation structure are important for the post-ECAP yielding and the following hardening response. Furthermore, the precipitates of the alloy clearly constrain the interactions of dislocations in work-hardening stage III—causing lower strain rate sensitivity and retarding the process of grain refinement as well. If compared to the pure aluminum, the precipitates avoid hardening in stage V where an additional rate and temperature-dependent effect contributes—supposedly caused by the interaction of deformation-induced vacancies and dislocations.

Introduction

When dealing with the work- or strain-hardening behavior of metals, the main intention is the description of the (true) flow stress as a function of plastic strain, temperature, and strain rate. Nowadays it is well established that the flow stress of polycrystalline face-centered cubic (fcc) metals is determined (contrary to body-centered cubic materials with a high Peierls stress) primarily by the number of dislocations and their athermal and thermal activated interactions [1]. The concept of dislocations, explaining the ductility of metals, was introduced by Orowan, Polanyi, and Taylor already in the early 1930s [2–4]. Based on the underlying microstructural processes, three deformation stages were introduced [5–8]. It is important to note that the contribution of an athermal and a (stacking fault and) temperature-dependent portion (thermally activatable) to the flow stress was already widely accepted. While these early investigations were performed mostly on pure single crystals in order to measure the intrinsic behavior of metals, it was shown later, that the features of work-hardening in (pure) polycrystals are very similar to that found in single crystals [9, 10].

Accordingly, the true stress–strain curves display a subdivision into three parts, starting with a flat slope followed by a very steep slope representing stages I and II, respectively. The steep slope in stage II results from multiple slip causing a pronounced multiplication and storage of dislocations in bundles or networks. These processes were found to be independent of temperature and strain rate [1]. In the following stage III the increase of flow stress is reduced and becomes nonlinear. This behavior is attributed to the temperature and strain-rate-dependent cross-slip of screw dislocations bypassing the heads of piled up dislocation groups. Moreover, the dislocations with opposite sign are increasingly annihilating, which causes dynamic recovery. As shown by Mughrabi [11] and Prinz et al. [12] the evolving microstructure is characterized by dense dislocation layers (cell walls) or sharp slip bands alternating with dislocation free zones oriented parallel to the direction of slip. The characterization of the stage III

M. Hockauf (✉)
Chemnitz University of Technology, Institute of Materials Science and Engineering, Erfenschlager Str. 73, 09125 Chemnitz, Germany
e-mail: matthias.hockauf@mb.tu-chemnitz.de

L. W. Meyer
Nordmetall Research and Consulting GmbH, Hauptstraße 16, 09221 Adorf (Neukirchen), Germany

work-hardening behavior can easily be performed by tensile or compression tests, while the latter are applicable for strains up to ~ 1.

Detailed information on the work-hardening behavior and the corresponding microstructural processes at even higher strains, as introduced by methods of severe plastic deformation (SPD), are available since the early 1990s, where two new stages were identified and added to the existing. According to the investigations of Zehetbauer et al. [13], Argon et al. [14], and Les et al. [15] stage IV shows (analogous to stage II) a linear work-hardening due to an additional increase of dislocation density. It is assumed that screw dislocations are trapped inside of the cell walls during intercellular slip [14]. This leads to a decomposition of the dislocations in partials with screw and edge character. This mechanism increases the misorientation of neighboring cells and forms grain boundaries, whereby the cell or grain size remains unchanged. As the storage has athermal character and the cross-slip, originating from stage III, proceeds, the thermally activatable flow stress contribution remains constant. With the onset of stage V, which is not generally accepted yet, the flow stress approaches saturation. It is assumed that the density of deformation-induced vacancies starts to increase by the onset of stage V. This enables climbing of edge dislocations and a further increase of grain boundary misorientations. Because the diffusion of these vacancies is temperature and strain-rate dependent, the thermally activatable contribution of the flow stress increases (analogous to stage III). Corresponding to the described work-hardening behavior, Fig. 1a shows a schematic stress–strain curve typical for fcc metals up to saturation. In order to separate the different stages the work-hardening rate ($\Theta = \mathrm{d}\sigma/\mathrm{d}\varepsilon$) as well as the strain-rate sensitivity (SRS—$m = \mathrm{d}\ln\sigma/\mathrm{d}\ln\dot{\varepsilon}$) are typically plotted as a function of the stress, Fig. 1b. It is important to note that the appearance and magnitude of these stages depends on the temperature and the material.

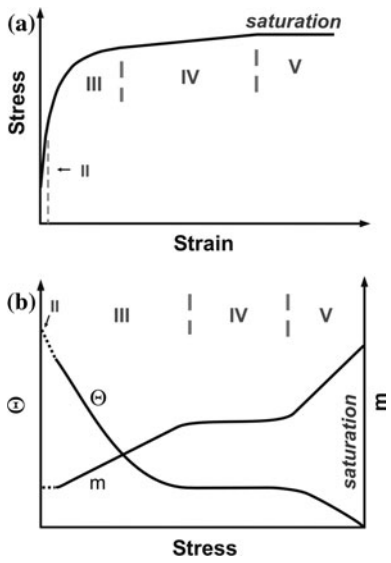

Fig. 1 Schematic plots of the work-hardening behavior up to very high strains, typical for polycrystalline fcc metals: **a** stress–strain curve, **b** the corresponding work-hardening rate Θ and strain rate sensitivity m

One of the most active and developing fields in materials science is the processing of bulk ultrafine-grained (UFG) materials by methods of SPD [16]. Equal-channel angular pressing (ECAP) [17] is the most developed SPD processing technique today. In principle a billet is pressed through a rigid tool constrained within an angled channel. Thereby a simple shear strain is introduced into the material. Since the cross-section of the billet remains practically unchanged, the pressings can be repeated in order reach extreme high cumulative strains. As shown by a review of Wei [18] the SRS of SPD-processed UFG fcc metals is significantly increased due to the abovementioned mechanisms. These investigations were done basically on (technical) pure metals or alloys with coarse incoherent particles which have a minor effect on mechanical properties. The scope of the present investigation is to evaluate the effect of fine coherent precipitates on the late (cold) work-hardening stages IV and V. ECAP is used to process the peak-aged aluminum alloy to different pre-strains before quasi-static and dynamic compression tests are performed. Technical pure aluminum is considered as reference.

Experimental

For the investigations two aluminum wrought materials of commercial purity were used. The pure aluminum AA1070 (0.06 wt% Si–0.19 wt% Fe–bal. Al) was supplied in the form of extruded cylindrical bars with a diameter of 25 mm. The material was machined into square-shaped billets and tempered at 360 °C for 20 min to remove any effect of cold working (soft annealed temper—O). The AA6060 (0.43 wt% Si–0.52 wt% Mg–0.16 wt% Fe–bal. Al) was supplied in the form of extruded square bars with an edge length of 15 mm. To achieve maximum strength a solid-solution heat treatment at 525 °C for 60 min was conducted, followed by water quenching and aging at 170 °C for 10 h (peak-aged temper—T6). The two materials were multi-pass ECAP processed at room temperature (RT) in a tool with a channel cross-section of 15×15 mm^2, an angle of 90° between the two intersecting channels, resulting in an equivalent plastic strain of 1.15 per pass [19]. The friction conditions inside the tooling are optimized by two sliding walls in the inlet channel and a bottom slider in the outlet channel following a concept proposed in [20]. The pressings were done with a

Table 1 Investigated conditions

N	φ_N	Condition
AA1070		
0	0	1070-O
2	2.3	1070-O, E2
8	9.2	1070-O, E8
AA6060		
0	0	6060-T6
2	2.3	6060-T6, E2
8	9.2	6060-T6, E8
16	18.5	6060-T6, E16

N, number of ECAP passes; φ_N, resulting equivalent plastic strain [19]

speed of 25 mm min^{-1} following route E. This hybrid route combines the classical routes C and B_c and provides an optimum of fully worked volume and rapid grain refinement [21]. To ensure homogeneous plastic flow without strain localization or cracks, and to avoid the formation of a corner gap, a backpressure of 85 MPa (19.1 kN) was applied via the bottom slider. The high quality of the samples processed by this tool was shown in [22] for RT-ECAP of an AA6082-T6. Table 1 shows the conditions that were considered in the present study. They were chosen because they represent different characteristic stages of grain refinement [23] and thus a characteristic work-hardening behavior is expected.

The characterization of the microstructure was done parallel to the flow plane (Y). The CG materials were investigated by optical microscopy. Therefore, the samples were polished and etched for ~15 s in a solution of 100 ml H_2O, 6 ml HCl, 2 ml H_3PO_4, and 12 ml HF at RT. The microstructure of the ECAP processed conditions was investigated by low-voltage scanning transmission electron microscopy (STEM) in a NEON40 field emission microscope from Zeiss. As shown in [24] STEM is an appropriate method to visualize the dislocation and grain boundary structure of UFG aluminum alloys. Thin slices where cut from the Y-plane of the billets, mechanically ground to a thickness of ~80 μm and further electrochemically thinned using a Tenupol-5 twin-jet polisher from Struers (with A7-electrolyte). Finally, the thickness of the oxide layer was reduced by ion milling with an angle of ~5° at 3 kV in a PIPS from Gatan. The transmission was performed with an acceleration voltage of 30 kV. Reference investigations were performed using the detector for secondary electrons (SE). The average grain size d was measured by the line interception method according DIN EN ISO 643. The average aspect ratio s represents the relation of the long to the short axis of the grains.

Cylinders with a diameter of 4.2 mm were extracted along the pressing direction by wire electro-discharge machining. The cylinders where surface-finished by external cylindrical grinding to the final diameter of 4 mm in order to remove the heat-affected zone. The compression specimens were obtained by cutting the cylinders followed by grinding the front faces in a special mold. With this procedure a final specimen length of 4 mm with a smooth surface and accurate rectangular shape was obtained. In the early stages of plastic flow, the strain measurement was done by strain gauges applied to the specimens. The given yield stress (YS) corresponds to a plastic strain of 0.2%. After loosing the signal from the strain gauges (at strains of ~0.1) the data captured by the displacement transducers of the particular test equipment were used. For the evaluation representative stress–strain curves from at least three replicates were selected. As the quality of measurement as well as the selection of an appropriate measuring technique are challenging tasks for producing reliable material data, different testing set-ups were used to investigate the material behavior over a wide range of strain rates. Tests at quasi-static (3×10^{-4} s^{-1}) and elevated (1×10^{0} s^{-1}) rates were performed in mechanical and servo-hydraulic machines from Zwick-Roell and Instron, respectively. For higher rates a drop tower (1.7×10^{2} s^{-1}) and a split Hopkinson pressure bar set-up (2.8×10^{3} s^{-1}) were used. The given (initial) strain rates represent the slope of the linear parts of the strain–time records of the strain gauges beyond the onset of plastic deformation. Further information on the test equipment for higher rates as well as the capturing and evaluation of the data is presented elsewhere [25, 26]. All compression tests were performed at RT. The front faces of the specimens were lubricated with high performance MoS_2 grease to minimize friction.

Results

Mirostructure—AA1070

The microstructural analysis by classical optical microscopy of the CG 1070-O gives an average size of 390 μm. A broad scatter in grain size ranging from smaller than 50 μm (3%) up to larger than 500 μm (9%) is typical for pure aluminum. The recrystallization produced an equiaxed grain shape ($s = 1.4$). Optical microscopy is not suitable for a proper characterization after ECAP processing. Figure 2 shows a STEM dark field micrograph of the condition 1070-O, E2. As illustrated above, the grain refinement is based on the multiplication and accumulation of dislocations forming cells and cell walls in work-hardening stage III. The clearly separated grains with sharp contrasts verify that this stage has been already exceeded and

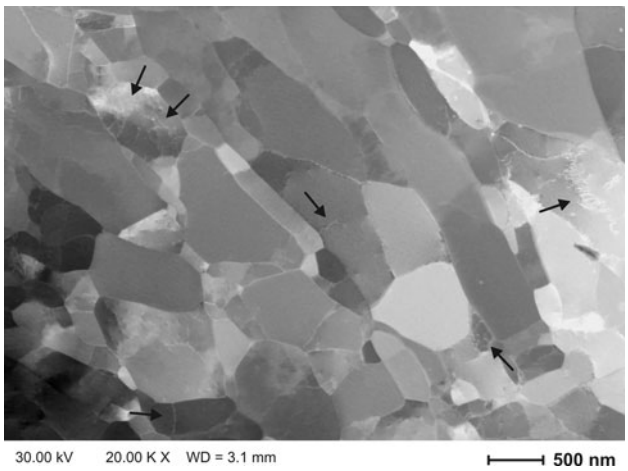

Fig. 2 STEM dark field micrograph of UFG 1070-O, E2 with elongated grains and a low number of dislocations (*small arrows*)

hardening in stages IV and V proceeded. The straining to $\varphi_2 = 2.3$ produced elongated ($s = 2.4$) ultrafine grains with an average size of 660 nm. It is important to note that the grain interior shows a rather low dislocation density (small arrows indicate the contrast of dislocations), suggesting that their interactions with grain boundaries during ECAP are significant. Below a certain cell or grain size this process is favored over their storage in the interior for pure metals, supporting the findings of Mughrabi [11] and Prinz et al. [12]. From Fig. 3a, b, showing the identical spot in STEM bright field- and SE-contrast, respectively, one can extract qualitative information on the grain misorientations. Some of the boundaries that are clearly visible by STEM, give no or only a very weak SE contrast (indicated by filled arrows). This is typical for LAGBs, which cause blurred transmission contrasts due to their high local stresses and corresponding alternating change in grain (cell) orientation [27–29]. Contrary to that HAGBs appear more distinct and as they separate grains with higher misorientations they are also detectable by SE or back scatter electron contrast (hollow arrows). Due to the low number of HAGBs, the condition AA1070-O, E2 is considered to represent an early stage of the grain refinement process.

Figure 4 shows the microstructure after a strain of $\varphi_8 = 9.2$ showing also a very low number of dislocations (small arrows). The average grain size remained constant at 660 nm during cold working beyond $\varphi_2 = 2.3$, while the aspect ratio was reduced slightly to 1.9. The sharp contrasts indicate that the fraction of HAGB increased significantly, if compared to AA1070-O, E2. Accordingly the condition AA1070-O, E8 represents a fully refined microstructure with a considerably high number of HAGBs. These findings are in good agreement with the theory of grain refinement by SPD [11–15, 30]. The microstructural

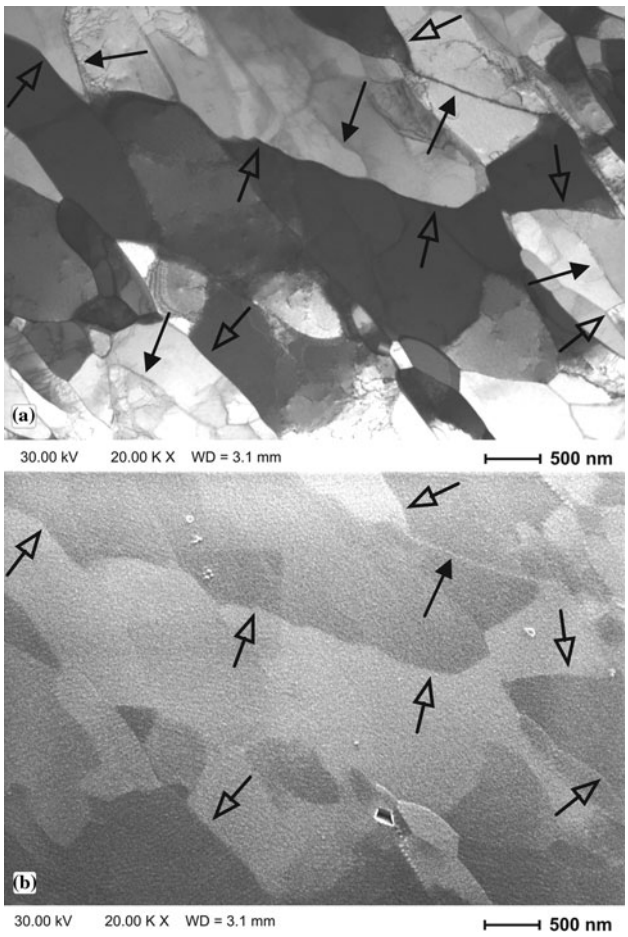

Fig. 3 Micrographs of UFG 1070-O, E2 **a** STEM-contrast—bright field, **b** SE-contrast with LAGBs (*large filled arrows*) and HAGBs (*large hollow arrows*)

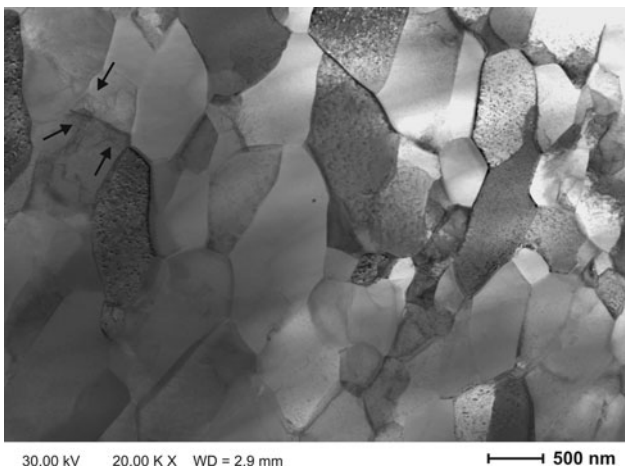

Fig. 4 STEM bright field micrograph of UFG 1070-O, E8 with slightly elongated grains and a low number of dislocations (*small arrows*)

features of the investigated conditions of the pure aluminum are summarized in Table 2. After ECAP processing no grains larger than 2 μm were detected.

Table 2 Microstructural features of the investigated conditions of the pure aluminum

1070-O	CG $d = 390$ μm, equiaxed $s = 1.4$
	Primary HAGBs
	Very low dislocation density
1070-O, E2	UFG $d = 660$ nm, elongated $s = 2.4$
	Many LAGBs with dislocations, few HAGBs
	Low dislocation density in the grain interior
1070-O, E8	UFG $d = 660$ nm, slightly elongated $s = 1.9$
	Many HAGBs, very few LAGBs
	Low dislocation density in the grain interior

Mirostructure—AA6060

The average grain size of the 6060-T6 CG condition is 120 μm with a distribution ranging from smaller than 25 μm (9 %) to larger than 200 μm (15%) with a rather equiaxed shape. A characterization of the microstructure by optical microscopy also reveals the presence of (primary) Fe-rich impurity phases with a size of 1–10 μm. As shown by the STEM micrograph in Fig. 5, smaller rod-shaped impurities (secondary phases) with a length and diameter of 250 and 75 nm, respectively, are also present. Such impurities are typical for commercial aluminum materials. They have only a minor effect on the mechanical properties. The coherent needle-shaped β'' zones produced by the age hardening exert the strengthening effect. These particles have a diameter of $\sim$4 nm and a length of $\sim$30 nm [31]. Their symmetrical orientation along the $\langle 100 \rangle$ Al planes is indicated by the darker (noisy-like) orthogonal stress contrasts (marked by ovals). In plane-oriented needles cause point-like contrasts (marked by circles).

For describing the microstructure after ECAP the interaction of the precipitates and dislocations is important. It was shown for a commercial 6082 that the β'' zones break-up due to the deformation and their length is shortened to about 4–8 nm while their diameter remained unchanged [32]. This suggests that the precipitates are fragmented by shearing into smaller pieces or might also get totally dissolved as shown in [33]. Based on these results it is assumed that the size of the β'' zones is reduced with increasing ECAP strain. As the resolution and magnification of the used STEM-technique is too low to characterize the morphology of the particles, they will be referred to as (sheared) precipitates further on.

Figure 6 shows a STEM micrograph of the condition 6060-T6, E2. It is easy to observe that the grain refinement is essentially modified by the presence of the precipitates when compared to the pure aluminum. The straining to $\varphi_2 = 2.3$ gives a bimodal grain size distribution consisting of $\sim$80% UFG regions with an average grain size of 510 nm embedded into a ribbon-shaped matrix of $\sim$20% dislocation cells with an average size of 1.8 μm. This suggests that the macroscopically homogenous straining spreads on the microstructural level into areas with higher (ultrafine grains) and lower straining (cells). As shown by Hughes et al. [30] this behavior is typical for the beginning of grain refinement in early stage IV. Attributed to the accumulating and pinning effect of the precipitates, the general dislocation density is much higher compared to the corresponding microstructure of AA1070, E2. This is especially true for the grain interiors. As a

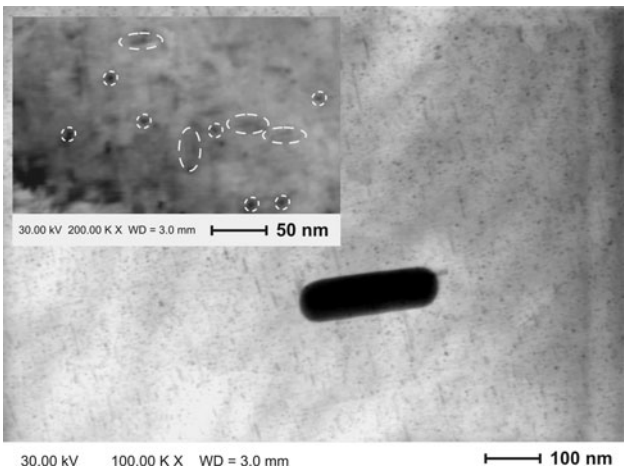

Fig. 5 STEM bright field micrographs of UFG 6060-T6—the detail represents maximum magnification wherein the ovals/circles mark needle-shaped β'' precipitates in length/crosswise orientation along $\langle 100 \rangle$ Al

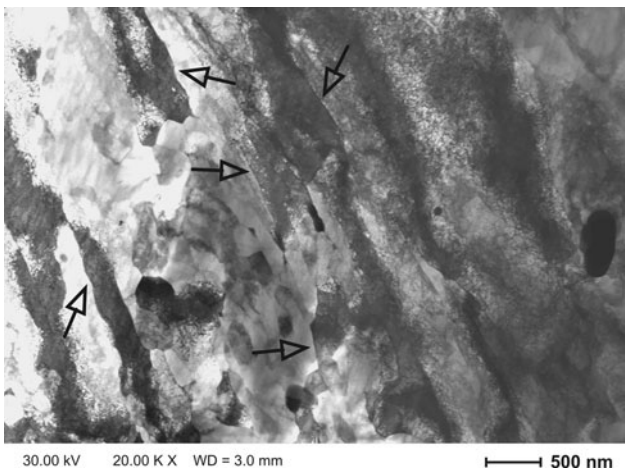

Fig. 6 STEM bright field micrograph of UFG 6060-T6, E2 showing an elongated bimodal microstructure with $\sim$80% UFG regions embedded into a ribbon-shaped matrix of dislocation cells separated by HAGBs (*large hollow arrows*)

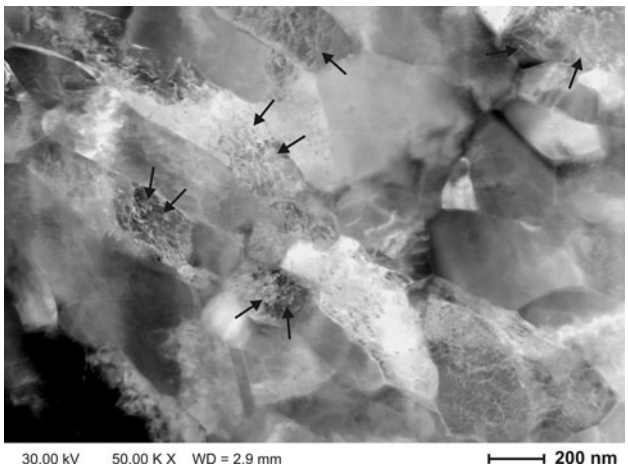

Fig. 7 STEM micrograph of UFG 6060-T6, E8 with homogenous ultrafine slightly elongated grains in dark field contrast (*small arrows* point to dislocations)

Table 3 Microstructural features of the investigated conditions of the aluminum alloy

6060-T6	CG $d = 120$ µm, equiaxed $s = 1.2$
	Primary HAGBs
	Very low dislocation density
6060-T6, E2	Bimodal—~80% UFG and ~20% dislocation cells
	UFG: $d = 510$ nm, elongated $s = 2.4$, many LAGBs and few HAGBs
	High dislocation density in the grain interior
	Cells: $d = 1.8$ µm, ribbon-shaped $s = 8.0$, many LAGBs and few HAGBs
	High dislocation density in the cells
6060-T6, E8	UFG $d = 310$ nm, slightly elongated $s = 2.0$
	Many HAGBs, few LAGBs
	High dislocation density in the grain interior

consequence of this relative higher storage activity, the increase of boundary misorientations is retarded and the frequency of intergranular slip is much smaller. Thus, the fraction of HAGBs (large hollow arrows) is much lower if compared to the pure aluminum, which represents a comparatively earlier phase in the refinement process.

The pinning effect of the precipitates on dislocations persists even after $N = 8$, producing also high dislocation densities inside of the grains (small arrows), see Fig. 7. The clear boundary contrasts indicate that primarily high grain misorientations coexist. The measured average grain size is 310 nm with a slightly elongated shape ($s = 2.0$). No grains larger than 1 µm were detected. For the condition 6060-T6, E16 no investigations on the microstructure were performed. From results in the literature [34, 35] no further significant grain refinement beyond $\varphi_8 = 9.2$ (or below ~300 nm) is expected. In contrast to that, boundary

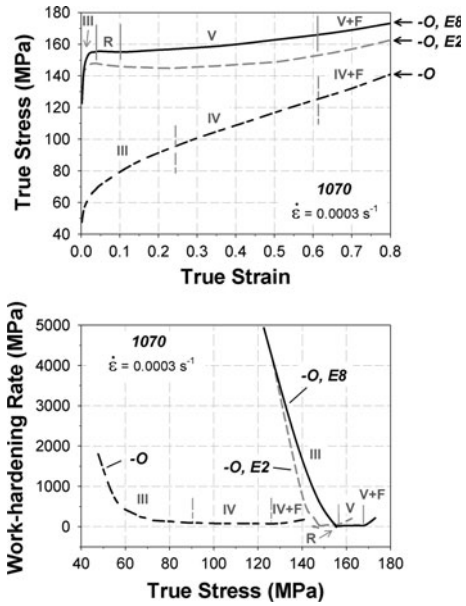

Fig. 8 Flow stress- and work-hardening behavior of 1070 from quasi-static compression tests where the hardening stages are marked for the conditions O and O, E8; *R*—rearrangement of the dislocation structure, *F*—increasing contact friction

misorientations will increase further as long as dislocation and vacancy activity proceeds. Table 3 summarizes the microstructural features of the investigated conditions of the aluminum alloy.

Work-hardening behavior—quasi-static loading

The true stress–strain curves as well as the derived work-hardening behavior of the pure aluminum at quasi-static loading are shown in Fig. 8. The plastic deformation of the CG condition 1070-O begins slightly below a stress of 50 MPa in stage III with a work-hardening rate of 1,800 MPa. The instantaneous decrease of Θ indicates that the fraction of dislocation annihilations by (thermally activatable) cross-slip increases. Stage IV sets in at a stress of 90 MPa wherein Θ remains constant at 80 MPa. At a stress of 125 MPa the lubrication film collapses, resulting in an abnormal increase of σ and Θ (*F*—influence of abnormal contact friction). It is important to note that contact friction is present in compression testing from the beginning of plastic deformation. This effect is—depending on the lubricant, tested material, and aspect ratio of the specimens—negligible and almost constant for strains up to ~0.4 to ~0.6 in the actual case [36]. Thus, the work-hardening rate (indicated by the slope of the σ–ε curves) is considered to be friction independent.

The UFG condition O, E2 exhibits a YS of 125 MPa. If compared to the maximum stress of ~140 MPa reached by

the CG condition O after a strain of only 0.8 this appears contradictory. According to the abovementioned theory of work-hardening the yielding of SPD-processed metals is expected to continue in stages IV or V. This is doubtlessly supported by the micrographs in Figs. 2, 3. However, the strong and rapid hardening to a stress of 148 MPa indicates the presence of stage III hardening and thus (athermal) dislocation storage, respectively. The reason for the apparent decrease of dislocation density can be found by two approaches.

Zehetbauer et al. [37, 38] showed that the dislocation density is pressure dependent, where higher pressures generate higher densities. Because the in situ measured flow stress in high-pressure torsion experiments was higher at higher axial forces (pressures), they suggested that a certain number of dislocations annihilate or rearrange statically already during unloading after SPD deformation. In order to verify this assumption for the ECAP processed aluminum materials an interrupted compression test was performed. A first compression loading was done beyond stage III up to a strain of $\sim$4% in order to reproduce a stage IV dislocation structure similar to that during ECAP. Subsequently the specimen was unloaded for $\sim$5 min in order to release the pressure, permitting annihilations, and than reloaded again. The procedure was repeated at a strain of $\sim$8%. As the flow stresses resumed at identical stress levels after reloading, significant static annihilation effects are considered to be unlikely.

Another approach for explaining the behavior is the consideration of the change in strain path from simple shear during ECAP to compression. This was found, for example, by Mingler et al. [39] and Yapici et al. [40]. They showed for pure Cu that a change in strain path causes a rearrangement of the ECAP microstructure wherein the grains partially dissolve by rebuilding of new ones according to the new strain path. This results in dislocation storage on the newly activated slip systems that are responsible for the stage III effect. From Fig. 8, it is also shown that beyond the hardening in stage III work-softening occurs. This can also be explained by the rearrangement of the microstructure, since the local grain boundary misorientations change simultaneously. Consequently, pre-existing dislocations pass through formerly unfavorably oriented barriers (cell walls or LAGBs) and cause the decrease in stress. Beyond the microstructural rearrangement (marked by *R*) the hardening proceeds. The very low work-hardening rate of 10–20 MPa indicates that the density of dislocations and vacancies is close to saturation, which suggests the presence of stage V. The clarification of this assumption follows in the next section by the application of higher strain rates. In case of stage V hardening particularly high SRS is expected. The UFG condition O, E8 shows an analogous behavior, although the rearrangement of the microstructure as well as the subsequent hardening occurs at slightly higher stresses.

If compared to the pure aluminum, the alloy shows a qualitatively similar flow stress behavior, whereas the presence of precipitates results in higher stresses, see Fig. 9. The strength increase from T6, E8 to T6, E16 indicates that the capacity for hardening is not exhausted at $\varphi_8 = 9.2$. This is in accordance with the results of Richert et al. [41], where the saturation on a cyclic extrusion- and compression-strained AlMg5 was identified beyond a strain of $\sim$11. Because of the higher stresses the undesired contact friction becomes noticeable already at a strain of $\sim$0.4.

The plastic deformation of the CG condition T6 begins at a stress of 205 MPa and reaches the end of stage III at $\sim$265 MPa. Compared to the 1070-O where the stress was doubled in this stage, the relative strength increase of the alloy is much lower. The following work-hardening rate of 80 MPa in stage IV is identical with that of the pure aluminum. This leads to the assumption that the characteristic trapping of screw dislocations during intercellular slip is not influenced by the precipitates. Due to the high dislocation density and the corresponding short glide paths the work-hardening rates for the UFG conditions of the alloy

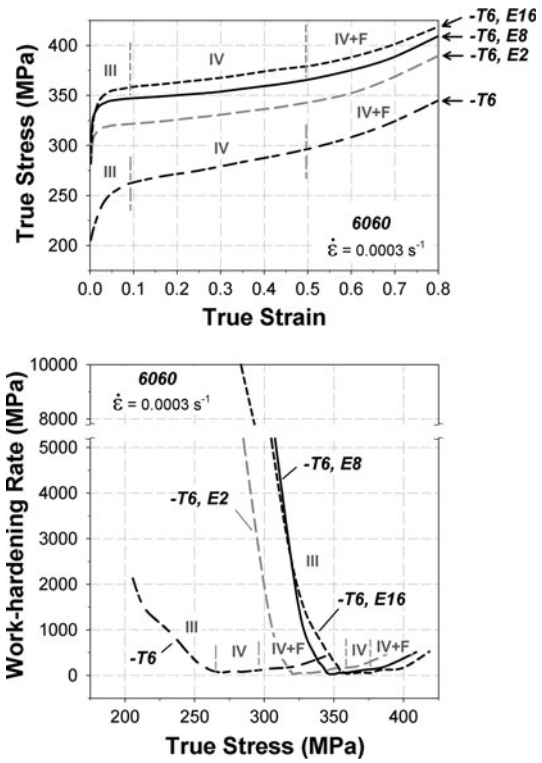

Fig. 9 Flow stress- and work-hardening behavior of 6060 from quasi-static compression tests where the hardening stages are marked for the conditions T6 and T6, E16; *R*—rearrangement of the dislocation structure, *F*—increasing contact friction

are $\gg$2,000 MPa. A pronounced rearrangement of the microstructure is not clearly detectable—but indicated by a temporary low Θ of $\sim$30 MPa. This result shows that the precipitates stabilize the initial UFG microstructure during strain path changes by constraining dislocation interactions and preventing from work-softening. Thus, strain localizations or necking during other forming operations is expected to be more effectively retarded for alloys. During the following straining the work-hardening rate is 40–50 MPa for all UFG conditions. As this value is approximately double as high as the Θ_V of the UFG 1070, it is temporarily ascribed to stage IV. Because the precipitates retard effectively dislocation interactions it is assumed that (athermal) stage IV hardening is effectively extended to higher strains and thus the (thermally activatable) deformation-induced vacancies might have a minor effect.

Work-hardening behavior—high strain rates

Figure 10 shows the influence of strain rate on the CG and UFG conditions after $\varphi_8 = 9.2$, wherein the σ–ε curves at quasi-static (3×10^{-4} s^{-1}) and at highest rates (2.8×10^{3} s^{-1}) are plotted. The stresses of the CG conditions are almost strain rate insensitive at the beginning of deformation. With increasing strain the stresses are increasing for dynamic loading, since the thermally activatable recovery by cross-slip of screw dislocations is suppressed. As shown by Meyer [42] and Kendall [43] the temperature and strain rate are replaceable parameters

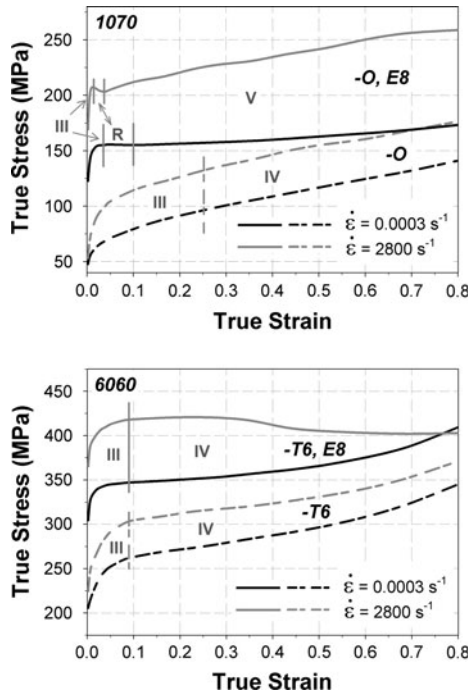

Fig. 10 Flow stress of the investigated materials in the CG and UFG conditions after $\varphi_8 = 9.2$ at quasi-static and dynamic loading

regarding the thermal activated movement of dislocations. This is a result of the decreasing probability (shortening of the "waiting-time") of dislocations to overcome the energetic barrier by the help of thermal activation [1, 5]. Thus, a test at RT with a high strain rate can result in the same thermal activation (or flow stress) as a test at lower temperature at quasi-static conditions. The onset of the following stage IV results in the same hardening response as no further thermally activatable effects contribute.

High rate testing is connected to adiabatic effects as soon as the plastic work converted into heat remains inside of the sample. According to Zehnder et al. [44] a compression test of aluminum with a 4 mm long specimen can be considered as quasi-adiabatic when the strain rate is higher than 150 s^{-1}. This is true for the drop tower and Hopkinson experiments where a strain of 0.8 is reached in $<$5 and 0.3 ms, respectively. With a Taylor–Quinney-factor of $\eta = 0.9$, this results in a temperature rise of $\sim$40 K (e.g., for 1070-O, E8) following Eq. 1, wherein ρ represents the density and c represents the specific heat

$$\Delta T = \frac{\eta}{\rho \cdot c} \int_{\varepsilon_0}^{\varepsilon_1} \sigma \mathrm{d}\varepsilon \tag{1}$$

As described above, this rise in temperature has no influence on the stress–strain response of the CG 1070-O, see Fig. 10. On the contrary, the stress slightly decreases for the CG 6060-T6 at higher strains where the temperature rises after $\varepsilon = 0.8$ for $\sim$100 K. The changing thermodynamic conditions are neglected for the following considerations, because the temperature rise is below 50 K up to strains of 0.35 (used in max. for evaluations) in general and thus only minor influences are expected.

Due to the high number of dislocations the dynamic loading of the UFG conditions results in an elevated stress already at the beginning of plastic deformation. The stage III hardening in combination with the rearrangement of the microstructure causes an upper YS phenomenon for the pure aluminum suggesting that the dynamic deformation produces an excess of dislocations that annihilate during the subsequent microstructural rearrangement. Beyond this point the stress further increases continuously almost linear if compared to quasi-static loading. This can be ascribed most likely to the effect of the suppressed thermally activatable diffusion of vacancies proving the presence of stage V for the pure aluminum. Beyond a strain of 0.8 the increase of stress resulting from stage V is almost equivalent to the portion generated in stage III. On the contrary, the UFG alloy hardens exclusively in stages III and IV without an additional stress contribution from stage V. After reaching a maximum at $\varepsilon = 0.22$ the prevailing effect from the increasing temperature results in work-softening.

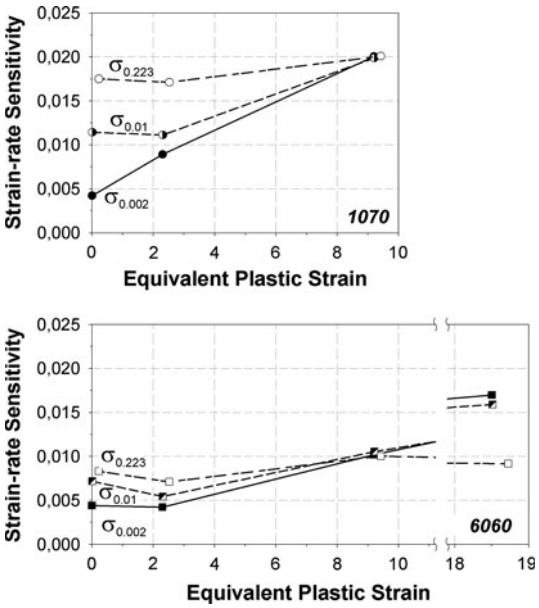

Fig. 11 Influence of SPD processing on the strain-rate sensitivity m of different flow stresses

The influence of the SPD processing on the SRS of three exemplarily chosen flow stresses (0.2, 1, and 20%) is shown in Fig. 11. The given m values were calculated by the least-square-fit method over the whole tested range of strain rates. The SRS of the YS ($\sigma_{0.002}$) is 0.004 for both materials. The straining of the CG 1070-O to 0.01 and 0.223 by compression increases the SRS remarkably to 0.011 and 0.018, respectively. Contrary to that a compression strain of 0.223 increases the SRS of the CG alloy to 0.008, which is less than half the increase if compared to the pure aluminum. The effect of SPD processing on the SRS is highest for the YS of the pure aluminum while the effect on the higher flow stresses declines. This is true in particular for the condition strained to $\varphi_2 = 2.3$, where the pronounced rearrangement of the microstructure leads to the same SRS. However, after $\varphi_8 = 9.2$ the SRS reaches 0.02 for all flow stresses. This suggests that the sources responsible for the production of thermally activatable interactions are somehow exhausted and thus saturation is reached. The 6060-T6 shows a qualitatively similar behavior up to $\varphi_8 = 9.2$, whereas the SRS reaches about half the values due to the retarding effect of the precipitates. The condition 6060-T6, E16 shows a specific feature since the stresses at the beginning of deformation ($\sigma_{0.002}$ and $\sigma_{0.01}$) are more sensitive than the later stresses after higher deformation ($\sigma_{0.223}$). This suggests that the extreme SPD pre-straining to $\varphi_{16} = 18.5$ caused an excess of dislocations that remain stabilized by precipitates. It is assumed that they rapidly annihilate during the subsequent compression along the new strain path. This effect might cause the dynamic decrease of the SRS.

Discussion

Chinh et al. [45] showed for ECAP processed Cu and Al that the evolution of the flow stresses σ can accurately be described by a modified Hollomon-type constitutive relationship, wherein σ_0 and σ_1 represent the YS and the maximum stress increase by work-hardening, respectively, see Eq. 2, wherein n and φ_c are constants.

$$\sigma = \sigma_0 + \sigma_1 \cdot \left[1 - e^{\left(-\frac{\varphi^n}{\varphi^c}\right)}\right] \quad (2)$$

In order to apply the so called CHL model to the investigated materials the quasi-static σ–ε data were used, whereas the SPD strain (φ_N) was added to the compressive strain (ε). Figure 12 shows that the model allows a good description of the global flow stress behavior over a wide range of strain. It is important to note that for the fitting at higher strains the data at the end of the σ–ε data was considered. The data influenced by surface friction was excluded. Accordingly, ECAP processing increases the YS of the AA1070-O by a factor of ~3.5, approaching a saturation stress of ~170 MPa. Due to the lower purity this value is ~50 MPa higher compared to the Al99.99 used in [45]. In contrast, saturation stresses of 170–180 MPa are reported by other authors [46–49] for similar processed Al99.5 with a slightly higher impurity content confirming the present results. The 6060-T6 reaches saturation at a stress of ~380 MPa after ECAP processing, being 1.9 times higher as the YS. Due to the difficulties of RT multi-pass ECAP processing of peak-aged aluminum alloys, much less results are available for comparison. Most authors use over-aged conditions in combination with elevated processing temperatures in order to reach sufficiently high strains. However, Chang et al. [50] processed a solution heat treated AA6005 to $\varphi_2 = 2.3$ and reported a maximum stress of 355 MPa. The CHL model for AA6060-T6 gives a ~20 MPa lower stress at that strain. Considering the higher Si-content (+0.2%) and the expected in situ aging of the AA6005, this is considered to give a sufficient correlation.

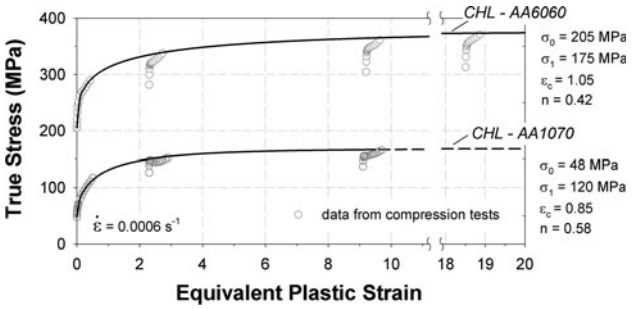

Fig. 12 Global flow stress behavior of the investigated materials over a wide range of strain using the CHL model [45] (including strain path changes)

For the discussion of the dynamic flow stress behavior the UFG conditions after $\varphi_8 = 9.2$ with a homogeneous microstructure and the CG conditions are considered. For the following examination, the flow stress σ is decomposed into an athermal contribution $\sigma_{ath(III,IV)}$ and two temperature and strain-rate-dependent contributions $\sigma_{th(III)}$ and $\sigma_{th(V)}$, generated in work-hardening stages III and V, respectively, see Eq. 3.

$$\sigma = \sigma_{ath(III,IV)} + \sigma_{th(III)} + \sigma_{th(V)} \quad (3)$$

This can be done on a qualitative basis by a direct comparison of the σ–ε curves at different strain rates. Figure 13a shows this for three characteristic strains for the pure aluminum. Accordingly, the temperature and strain-rate-dependent contribution at the onset of plastic deformation in stage III (III_b) is very low (5 MPa), showing that the quasi-static flow stress (athermally dominated) prevails. At the end of stage III hardening (III_e) the athermal dominated stress is increased due to dislocation storage. Similarly, the thermally activatable portion is increased to 40 MPa due to pronounced cross-slip activity. In stage IV (at $\varepsilon = 0.61$) the stress is increasing further while the thermally activatable portion remains constant at 40 MPa. This proves the athermal character of the hardening in stage IV. Due to the change in strain path the hardening of the 1070-E8 begins in stage III, whereas $\sigma_{th(III)}$ is increased to 45 MPa during ECAP processing. In the following rapid stage III hardening this portion increases to 52 MPa. Further straining leads to the development of an additional thermally activatable contribution and thus indicates the presence of stage V. After a compressive strain of 0.61 the temperature and strain-rate-dependent contribution is 87 MPa (50% of the quasi-static stress). Hence, the resulting contribution from stage V is 35 MPa.

The same analysis was done for the investigated alloy, see Fig. 13b. Here, the given thermally activatable contribution of 20 MPa increases to 40 MPa in stage III. Due to the more significant influence of adiabatic heating the hardening in stage IV was considered only up to a strain of 0.22. Analogous to the pure aluminum, ECAP processing increases $\sigma_{th(III)}$. Here, the values of 60 MPa at the beginning and 70 MPa at the end of stage III are reached, respectively. This is only 20% of the quasi-static stress. In contrast to the pure aluminum, this portion remains unchanged in the following stage IV even after extreme strains of $\varphi_{16} = 18.5$. Thus, the temperature and strain-rate-dependent contribution of the flow stress of the alloy is significantly lower and features of stage V hardening were not verified.

These findings can be explained by the presence of the sheared precipitates which supposedly have a twofold effect. It is assumed that they constrain dislocation interactions due to their pinning effect in stage III on the one hand. On the other hand it is assumed that their remnant stress fields effectively attract deformation-induced vacations, avoiding dislocation climb and thus the onset of stage V.

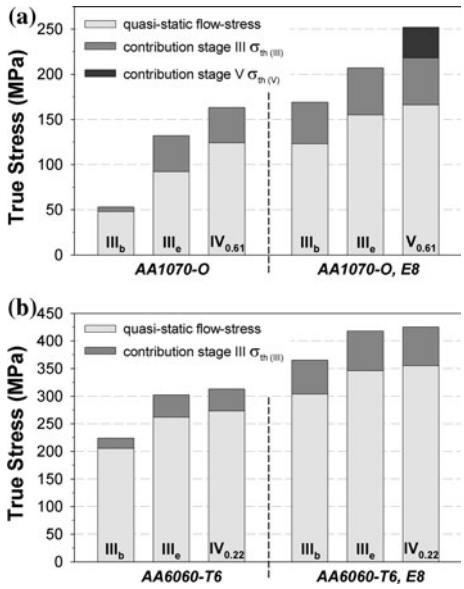

Fig. 13 Flow stress contributions for the CG and UFG conditions ($\varphi_8 = 9.2$) by comparing the σ–ε data at quasi-static and at highest rates of 3×10^{-4} and 2.8×10^3 s^{-1}, respectively, for **a** 1070-O and **b** 6060-T6

Summary and conclusions

The development of the microstructure and work-hardening behavior up to very high strains was characterized for two commercial aluminum wrought materials. In order to investigate the influence of coherent precipitates pure aluminum AA1070 (soft annealed) and the aluminum alloy AA6060 (peak-aged) were considered. Besides the CG conditions, the UFG conditions after ECAP processing to $\varphi_2 = 2.3$, $\varphi_8 = 9.2$, and $\varphi_{16} = 18.5$ were chosen as they represent different stages of grain refinement.

Room temperature ECAP processing to $\varphi_2 = 2.3$ produces an UFG microstructure for both materials, whereas the average initial grain size of >100 μm is reduced effectively below 1 μm. The grain boundaries have low angle misorientations transforming into HAGBs during further deformation. The average grain size of the pure aluminum after $\varphi_8 = 9.2$ is 660 nm and the grain interiors have a low dislocation density. Due to the pinning effect of the sheared precipitates the alloy shows a much higher dislocation density and reaches an average grain size of 310 nm for the same ECAP strain.

The flow stress behavior was measured by compression tests over a wide range of strain rates from 3×10^{-4} to 2.8×10^{3} s^{-1} in order to identify the work-hardening stages and the corresponding microstructural interactions on a qualitative basis. Both the CG and the UFG conditions of the two investigated materials show stage III hardening at the beginning of plastic deformation. Due to the increasing (temperature and strain-rate dependent) cross-slip activity, the SRS is increased significantly herein. The UFG conditions, which passed this stage already during the ECAP processing show also stage III hardening at the beginning of plastic deformation. This unexpected effect can be attributed to the change in strain path from simple shear to compression, where the newly activated glide systems presumably cause this effect. In this case stage III is shortened. Beyond stage III the CG conditions harden in stage IV wherein the stress increases on a very low rate due to the storage and decomposition of dislocations in the grain boundaries or cell walls. Because this effect has athermal character, the SRS remains constant. The UFG conditions of the alloy represent the same characteristic with a slightly reduced work-hardening rate independent of the pre-strain introduced by ECAP. The UFG conditions of the pure aluminum are an exception since stage III is followed by a rearrangement of the dislocation structure causing work-softening. It is assumed that this also can be attributed to the change in strain path. After that an additional temperature and strain-rate-dependent effect was identified, suggesting the presence of stage V and supporting the findings of [13–15]. Contrary, such a behavior was not found for the alloy, which suggests that the underlying mechanism of vacancy diffusion is influenced by the presence of the precipitates. It is assumed that the deformation-induced vacancies are absorbed in the (remnant) stress fields of these (sheared) precipitates so that (unlike the pure aluminum) they cannot attribute to temperature and strain-rate-dependent climb.

The (quasi-static) saturation stresses of the UFG pure aluminum and the alloy were identified to be 170 and 380 MPa, which is roughly 3.5- and 2-fold the YS of the CG unstrained conditions, respectively.

The current study suggests that the flow stress behavior of the investigated aluminum materials can be well described by the classical theory of work-hardening of polycrystalline fcc metals.

Acknowledgements The authors gratefully acknowledge the Deutsche Forschungsgemeinschaft (DFG) for supporting this work carried out within the framework of Sonderforschungsbereich 692—Hochfeste aluminiumbasierte Leichtbauwerkstoffe für Sicherheitsbauteile. Further thank goes to I. Dögel for his help with the ECAP processing and to A. Schulze for her support with the sample preparation and investigation of the microstructure by STEM.

References

1. Seeger A (1954) Philos Mag 45:771
2. Orowan E (1934) Z Phys 89:634
3. Polanyi M (1934) Z Phys 89:660
4. Taylor GI (1934) Proc R Soc Lond A 145:362
5. Seeger A (1958) In: Flügge S (ed) Handbuch der Physik VII 2. Springer, Berlin
6. Friedel J (1955) Philos Mag 46:1169–1186
7. Diehl J (1956) Z Metallkd 47:331
8. Hirsch PB, Mitchell TE (1967) Can J Phys 45:663
9. Knoell H, Macherauch E (1969) Z Metallkd 60:399
10. Mecking H, Kocks UF (1981) Acta Metall 29:1865
11. Mughrabi H (1983) Acta Metall 31:1367
12. Prinz FB, Argon AS (1984) Acta Metall 32:1021
13. Zehetbauer MJ, Seumer V (1993) Acta Metall Mater 41:577
14. Argon AS, Haasen P (1993) Acta Metall Mater 41:3289
15. Les P, Zehetbauer MJ, Rauch EF, Kopacz I (1999) Scr Mater 4:523
16. Valiev RZ, Estrin Y, Horita Z, Langdon TG, Zehetbauer MJ, Zhu YT (2006) JOM 58:33
17. Segal VM, Reznikov AE, Drobyshevskiy AE, Kopylov VI (1981) Russ Metall 1:99
18. Wei Q (2007) J Mater Sci 42:1709. doi:10.1007/s10853-006-0700-9
19. Iwahashi Y, Wang JT, Horita Z, Nemoto M, Langdon TG (1996) Scr Mater 35:143
20. Segal VM (2004) Mater Sci Eng A 386:269
21. Barber RE, Dudo T, Yasskin PB, Hartwig KT (2004) Scr Mater 51:373
22. Hockauf M, Meyer LW, Nickel D, Alisch G, Lampke T, Wielage B, Krüger L (2008) J Mater Sci 43:7409. doi:10.1007/s10853-008-2724-9s
23. Hockauf M, Meyer LW, Halle T, Kuprin C, Hietschold M, Schulze S, Krüger L (2006) Int J Mater Res 97:1392
24. Qian T, Marx M, Schüler K, Hockauf M, Vehoff H (2010) Acta Mater 58:2112
25. Meyer LW, Krüger L (2000) In: Kuhn HM (ed) Mechanical testing and evaluation, vol 8. ASM International, Materials Park
26. Gray GT III (2000) In: Kuhn HM (ed) Mechanical testing and evaluation, vol 8. ASM International, Materials Park
27. Wang N, Wang Z, Aust KT, Erb U (1997) Acta Mater 45:1655
28. Dalla Torre F, Van Swygenhoven H, Victoria M (2002) Acta Mater 50:3957
29. Koneva NA (2006) In: Altan BS (ed) Severe plastic deformation: toward bulk production of nanocrystalline materials. Nova Science Publisher, New York
30. Hughes DA, Hansen N (1997) Acta Mater 45:3871
31. Matsuda K, Gamada H, Fujii K, Uetani Y, Sato T, Kamio A, Ikeno S (1998) Metall Mater Trans A 29:1161
32. Roven HJ, Liu M, Werenskiold JC (2008) Mater Sci Eng A 483–484:54
33. Gutierrez-Urrutia I, Muñoz-Morris MA, Morris DG (2005) Mater Sci Eng A 394:399
34. Pippan R, Wetscher F, Hafok M, Vorhauer A, Sabirov I (2006) Adv Eng Mater 8:1046
35. Kopylov VI, Chuvil'deev VN (2006) In: Altan BS (ed) Severe plastic deformation: toward bulk production of nanocrystalline materials. Nova Science Publisher, New York
36. Herzig N, Meyer LW, Halle T, Raschke S (2007) In: Vollertsen F, Yuan S (eds) Proceedings of the second international conference on new forming technology (ICNFT), Bremen, Germany
37. Zehetbauer MJ (2002) In: Zhu YT, Mishra RS, Semiatin SL, Saran MJ, Lowe TC (eds) TMS annual meeting, Seattle, WA

38. Zehetbauer MJ, Kohout J (2002) In: Khan AS, Lopez-Pamies O (eds) Ninth international symposium on plasticity and its current applications. NEAT Press, MD
39. Mingler B, Karnthaler HP, Zehetbauer MJ, Valiev RZ (2001) Mater Sci Eng A 319–321:242
40. Yapici GG, Beyerlein IJ, Karaman I, Tomé CN (2007) Acta Mater 55:4603
41. Richert M, Stüwe HP, Zehetbauer MJ, Richert J, Pippan R, Motz C, Schafler E (2003) Mater Sci Eng A 355:180
42. Meyer LW (1984) In: Harding J (ed) Institute of physics conference series. Institute of Physics, Oxford
43. Kendall DP (1972) Trans ASME D 94:207
44. Zehnder AT, Babinsky E, Palmer T (1998) Exp Mech 38:295
45. Chinh NQ, Horvath G, Horita Z, Langdon TG (2004) Acta Mater 52:3555
46. Höppel HW, May J, Eisenlohr P, Göken M (2005) Mater Res Adv Tech 96:566
47. Miyamoto H, Ota K, Mimaki T (2006) Scr Mater 54:1721
48. Wang M, Shan A (2008) J Alloys Compd 455:L10
49. Sun PL, Cerreta EK, Bingert JF, Gray GT III, Hundley MF (2007) Mater Sci Eng A 464:343
50. Chang JY, Shan A (2003) Mater Sci Eng A 347:165